Wide-field imaging of single nanoparticle extinction with sub-nm^2 sensitivity

Lukas M. Payne,[1] Wolfgang Langbein,[2,*] and Paola Borri[1]

[1] *School of Biosciences, Cardiff University, Cardiff CF24 3AA, United Kingdom*
[2] *School of Physics and Astronomy, Cardiff University, the Parade, Cardiff CF24 3AA, United Kingdom*

(Dated: December 30, 2017)

We report a highly sensitive wide-field imaging technique for quantitative measurement of the optical extinction cross-section $\sigma_{\rm ext}$ of single nanoparticles. The technique is simple and high-speed, and enables simultaneous acquisition of hundreds of nanoparticles for statistical analysis. Using rapid referencing, fast acquisition, and a deconvolution analysis, a shot-noise limited sensitivity down to 0.4 nm^2 is achieved. Measurements on a set of individual gold nanoparticles of 5 nm diameter using this method yield $\sigma_{\rm ext} = (10.0 \pm 3.1)$nm^2, consistent with theoretical expectations, and well above the background fluctuations of 0.9 nm^2.

I. INTRODUCTION

Small nanoparticles (NPs) in the sub-10 nm size range are increasingly important for many applications ranging from optoelectronic devices exploiting quantum confinement at the nanoscale [1], to drug delivery and diagnostics, since NPs of these sizes can be easily internalized by living cells via specific pathways, resulting in targeted delivery [2]. In this context, their optical response offers many opportunities in imaging and sensing. Increasing attention has been devoted recently to develop methods capable of detecting *single* NPs, since their properties can significantly differ from the ensemble average owing to inhomogeneities in NP size and shape. However, many NPs of widespread use are weakly or non-fluorescent, for example metallic NPs, making their optical detection in the sub-10 nm size range specifically challenging.

It is well known that NPs exhibit linear optical properties described by an absorption cross-section $\sigma_{\rm abs}$, a scattering cross-section $\sigma_{\rm sca}$, and the resulting extinction cross-section $\sigma_{\rm ext} = \sigma_{\rm abs} + \sigma_{\rm sca}$. These cross-sections are related to the size of the NP, with $\sigma_{\rm abs}$ and $\sigma_{\rm sca}$ scaling with the third and sixth power of the NP radius, respectively, for sizes much smaller than the light wavelength. Existing techniques able to detect $\sigma_{\rm ext}$ of individual particles include (for a recent review see Ref. 3) dark-field micro-spectroscopy, photothermal imaging (PTI) [4], spatial modulation micro-spectroscopy (SMS) [5], and laser-based transmission [6]. However, each method has limitations. PTI, SMS, and the laser-based transmission microscopy are point scanning techniques, therefore costly and less amenable to the rapid characterization of a large number of NPs compared to wide-field techniques. Additionally, PTI and SMS are modulation-based which requires specialized equipment such as acousto-optical modulators and lock-in detection, while laser-based transmission microscopy requires balanced photodiodes to reduce laser intensity fluctuations down to shot-noise. Dark-field micro-spectroscopy, is usually implemented in wide-field, but only measures $\sigma_{\rm sca}$, while PTI only measures $\sigma_{\rm abs}$. Furthermore, both require a calibration reference for quantification.

An important consideration for this work is the detection limit of these methods. Dark-field micro-spectroscopy is practically limited by scattering background from sample inhomogeneities or debris, typically limiting the sensitivity to $\sigma_{\rm ext} \approx 50\,$nm^2, equivalent to a single gold NP (GNP) of 20 nm diameter. Owing to their modulation-based approaches, SMS and PTI exhibit greater sensitivity, with SMS having been demonstrated on single GNPs down to 5 nm diameter ($\sigma_{\rm ext} \approx 10\,$nm^2) [5], and PTI down to 1.4 nm diameter GNPs ($\sigma_{\rm ext} < 0.7\,$nm^2) [4]. Single molecules with $\sigma_{\rm abs} \approx 0.1\,$nm^2, in a field of view of a few micrometers, have been seen with laser-based transmission [6, 7]. To quantitatively determine the cross-section, a subtraction of the sample background variations was used, exploiting specific responses of the molecule of interest, such as photobleaching, or spectral and polarization dependencies. This type of background subtraction is not generally applicable, and using sample scanning limits the speed for high throughput applications. A more detailed comparison between the scanning and widefield approach is given in appendix I.

In our previous work [8], we established a simple, wide-field technique capable of rapidly measuring $\sigma_{\rm ext}$ and $\sigma_{\rm sca}$ of hundreds of individual nanoparticles, in absolute units without the need of calibration standards. In Ref. 9 we showed a sensitivity of $\sigma_{\rm ext} \approx 5\,$nm^2. Here, we demonstrate a step-change improvement in sensitivity by an order of magnitude, taking it into the sub-nm^2 regime, through the use of rapid referencing, fast acquisition, and deconvolution, while keeping the simple wide-field approach.

II. SETUP AND SAMPLES

The experimental set-up is sketched in Fig. 1 and consists of an inverted microscope (Nikon Ti-U) equipped with a LED source (Thorlabs LED4D) of center wavelength $\lambda = 530\,$nm (chosen to be in resonance with the localized surface-plasmon absorption peak of a spherical GNP in the dipole limit [3]) with 30 nm full-width at half maximum (FWHM), an oil condenser of 1.34 numerical aperture (NA), a 100x 1.45 NA oil immersion objective with a 1.5x tube lens, providing a magnification of $M = 150$ on a monochrome scientific-CMOS (sC-

* Electronic address:langbeinww@cardiff.ac.uk

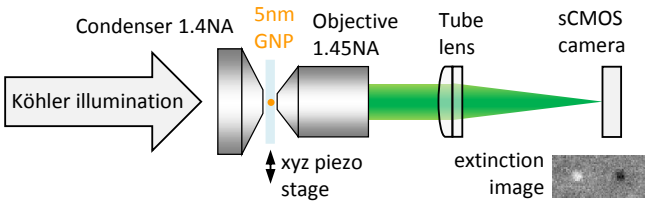

FIG. 1. Sketch of the imaging setup used. The transmission of a sample under Köhler illumination is imaged onto a sCMOS camera, using high numerical apertures. The sample position is laterally shifted by a piezoelectric stage for referencing.

MOS) camera (PCO Edge 5.5), with a full well capacity of $N_{\mathrm{fw}} = 30000$ photoelectrons, attached to the left port of the microscope. Images were taken in 16-bit Tiff format with 1280×512 pixel resolution to allow for a frame rate of ≈ 400 frames per second (FPS). The sample position on the microscope was controlled coarsely via a manual micrometer-controlled 2D translation stage (Mad City Labs Microstage-LT), and finely by a piezoelectric nano-positioning stage (Mad City Labs NanoLP200). To effectively show the enhanced sensitivity, we investigated GNPs of nominal 5 nm diameter (BBI Solutions) drop-cast onto a glass coverslip, covered in silicone oil (refractive index n = 1.518) and sealed onto a glass slide with clear nail varnish. GNPs of nominally 60 nm diameter (BBI Solutions) were drop-cast onto the same sample at about 1:5 relative concentration to the 5 nm GNPs, and provided objects easily visible in the transmission to aid finding the sample plane and optimising the focus.

III. DATA ACQUISITION

At root, the technique is a simple wide-field transmission imaging, with one measurement taken with the NPs in focus, and another taken with the NPs displaced, to act as a reference. After using a defocused reference [8], we adopted [9] a lateral shift by a small distance d (a few times the spatial resolution) from position $P_1 = (x_0, y_0)$ to position $P_2 = (x_0 + d, y_0)$. Reduction of shot noise was achieved through averaging of a large number N_{a} of individual acquisitions. We call the averaged intensities of the signal and reference images I_{S}, and I_{R}, respectively. The extinction image is then given by $\Delta = 1 - T$, with the transmission image $T = I_{\mathrm{S}}/I_{\mathrm{R}}$. At a framerate of 400 FPS, it takes about one minute to acquire 25600 frames. While this is a short overall experiment, I_{S} and I_{R} were sufficiently temporally separated to result in relevant drifts in the sensor electronics. This limited the achievable sensitivity, mostly due to a vertical stripe pattern appearing in the images, as well as some illumination drift during the experiment. The vertical striping can be seen in Fig. 2a. In order to reduce the sensitivity to below $5\,\mathrm{nm}^2$, this patterning needed to be suppressed.

Before discussing the suppression, we introduce the method used to quantify σ_{ext} of an individual NP from Δ. The extinction cross-section of a NP centred in an area A_{i}, of radius r_{i}, in the image, may be expressed as $\sigma_{\mathrm{ext}} = \int_{A_{\mathrm{i}}} \Delta dA$. Here, r_{i} has to be larger than the spatial resolution to give an accurate result. Choosing

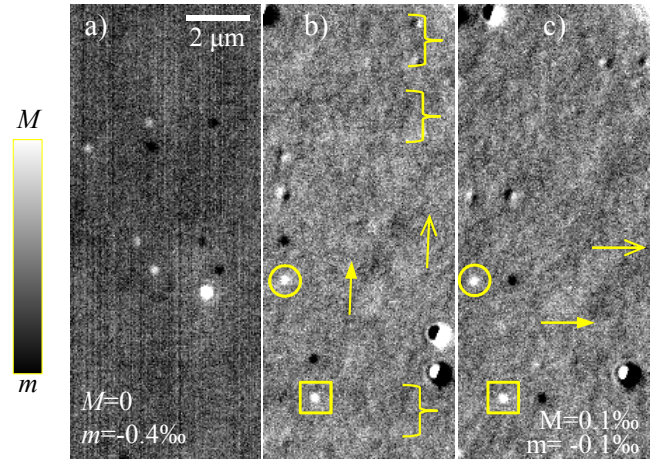

FIG. 2. Extinction images for different referencing of a sample with 5 nm GNPs. a) Δ_1 images for $N_{\mathrm{a}} = 25600$ and sequential referencing. b) Δ_1 image for rapid referencing, using $N_{\mathrm{d}} = 256$, and $N_{\mathrm{a}} = 128000$. Brackets guide the eye to residual banding. Circles and squares indicate identical particles, arrows indicate BG mottling along shift direction. c) as b), but using additional sample motion. Grayscale as indicated between m and M as given.

$r_{\mathrm{i}} \approx 3\lambda/(2\mathrm{NA})$, approximately at the second Airy ring of the objective point-spread function (PSF), yielded residual errors below a few percent [8]. To account for drift of the illumination intensity, residual influence of nearby NPs, or local inhomogeneity, we can determine a local background (BG) extinction $\Delta_{\mathrm{b}} = A_{\mathrm{b}}^{-1} \int_{A_{\mathrm{b}}} \Delta dA$. In Ref. 8 and 9, Δ_{b} was determined from the area A_{b} between the radius r_{i} and $2r_{\mathrm{i}}$, yielding the BG-corrected $\sigma_{\mathrm{ext}} = \int_{A_{\mathrm{i}}} (\Delta - \Delta_{\mathrm{b}}) dA$. While this is a generally applicable method, it adds noise to the measurement, depending on the size of the BG area. In Ref. 8 and 9, A_{b} was three times A_{i}, leading to a relative shot noise increase of about 15%, as discussed in appendix Sec. D. When using the shifted reference technique we can avoid an explicit BG-subtraction. In this case, we have two contrast images: Δ_1, using the particle at P_1 as I_{S} and at P_2 as I_{R}, and Δ_2, exchanging the roles of P_1 and P_2. Δ_1 has a bright spot at P_1, and a dark spot at P_2, as seen in Fig. 3a. We can therefore make two measurements of σ_{ext}, yielding $2\sigma_{\mathrm{ext}} = \int_{A_{\mathrm{i}}(P_1)} \Delta_1 \mathrm{d}A + \int_{A_{\mathrm{i}}(P_2)} \Delta_2 \mathrm{d}A$, where $A_{\mathrm{i}}(P_{1,2})$ are centred at $P_{1,2}$, respectively. The two regions serving as BG in $\Delta_{1,2}$ are shifted by $\pm d$ from the particle. This averaging of two independent measurements reduces the noise by a factor of $\sqrt{2}$. Assuming negligible BG gradients surrounding a particle, the part of σ_{ext} due to the local BG is of equal and opposite sign in $\Delta_{1,2}$, and the average of Δ_1 and Δ_2 removes its influence. The smaller the shift distance, d, the smaller the residual effect of the BG gradient. The minimum separation for which particle and BG regions do not overlap is $2r_{\mathrm{i}}$. In the data shown here we used $d = 1.25\,\mu$m, about 100 nm larger than $2r_{\mathrm{i}}$ for $\lambda = 550$ nm, and NA = 1.45.

To suppress the pattern noise seen in Fig. 2a we decreased the temporal separation between taking the data at the two positions $P_{1,2}$, and use $m \gg 1$ repeats to obtain a large number of frames. This rapid temporal referencing suppresses the effects of slow drifts of

the setup, which are firstly, a stripe pattern attributed to drifts of supply voltages and sensor temperature of the camera, and secondly, lamp intensity drift. In order to achieve this rapid referencing, we synchronously triggered the camera and stage via a home-built electronics and software. Briefly, the stage-camera system was triggered continuously with one trigger per $\tau = 2.6\,\mathrm{ms}$, each trigger eliciting a single acquisition by the PCO with 1.4 ms exposure time. The stage switched between positions P_1 and P_2, after a defined number of triggers N_d. We chose $N_\mathrm{d} = 256$, and averaged $N_\mathrm{s} = 128 = N_\mathrm{d}/2$ frames in software. Hence, the time between acquisition sets at P_1 and P_2 was only $t_\mathrm{d} = \tau N_\mathrm{d}/2 \approx 0.33\,\mathrm{s}$, about 200 times less than in Fig. 2a. Notably, this technique also augments our method with time-resolved extinction capability, with a time resolution of t_d. We used here $m = 500$ repeats, for a total acquisition time of $t_\mathrm{acq} = 2mN_\mathrm{d}\tau \sim 666\,\mathrm{s}$, resulting in $2m = 1000$ images of Δ stored for post-processing. Notably, during this acquisition period, the sample can drift laterally, on the scale of microns per hour. Hence, an in-house registration software was written, based on pattern recognition [10], to track the particles and shift the frames accordingly. The registration also allows combining data taken in sequential runs, for example to correct focus drifts. Once registered, the Δ images are averaged to produce a single final extinction image. The result can be seen in Fig. 2b, showing that the vertical striping has been removed.

However, weak bands running horizontally across the image in Fig. 2b can now be seen (see also the full size image in the appendix Fig. 7). These features, indicated by brackets enclosing their vertical extent, appear to be sensor fluctuations which occur within t_d. To suppress these structures, we implemented an additional motion of the sample, orthogonal to the displacement d, shifting the particle across the sensor to average these bands. To limit the total shift, we subdivide the repetitions into n cycles of k repetitions, $m = nk$, with positions $P_1 = (x_0, y_0 + ls)$, and $P_2 = (x_0 + d, y_0 + ls)$, with the counter $l = 0..k-1$ and the orthogonal shift distance per repetition s. Here we used $s = 43.3\,\mathrm{nm}$, corresponding to about one pixel in the image, hence covering a total distance of $ks \approx 2\,r_\mathrm{i} \approx 2170\,\mathrm{nm}$ in one cycle, roughly the vertical size of the banding pattern. The resulting Δ images are registered and averaged as before, resulting in the Δ_1 image given in Fig. 2c, free of sensor-based patterns. We note that this sample motion method can be employed generally for fixed pattern reduction.

IV. ANALYSIS

To investigate the lowest achievable exctinction cross-section noise, we consider its dependence on N_a. Without sensor patterning, we expect that the noise is limited by photon shot noise, which at signal levels above 10^4 electrons per pixel is dominating the sensor read noise of about 2 electrons. The mean image intensity was $I \approx 55000$ counts, which, using the measured camera gain $g = 0.5421$ photoelectrons per count, corresponds to $N_\mathrm{e} \approx 29816$ photoelectrons per pixel, close to N_fw.

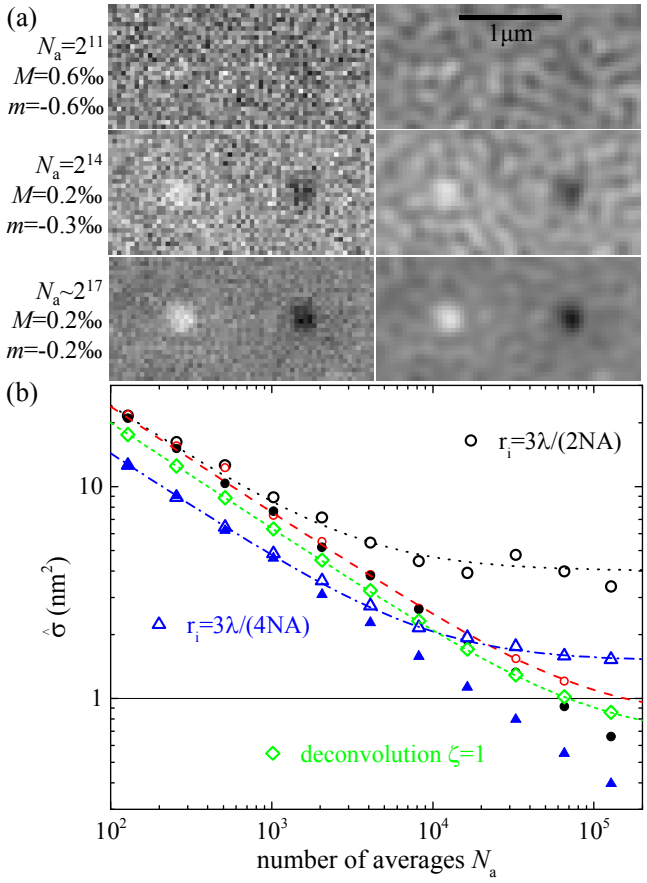

FIG. 3. Extinction images and scattering cross-section noise on a sample with 5 nm GNPs. (a) Left column: Δ_1 for a single 5 nm GNP with rapid referencing and sample motion, for increasing N_a as indicated. Right column: corresponding images excluding out-of-band spatial frequencies. Greyscale as in Fig. 2. (b) measured noise versus N_a. For $r_i = 3\lambda/(2\mathrm{NA})$: black disks – from out-of-band images, fitting to $\hat{\sigma}_\mathrm{n} = 238 N_\mathrm{a}^{-0.5}\,\mathrm{nm}^2$; red small circles – at fixed BG points for sequential acquisitions, with a fit (dashed red line) $\hat{\sigma}_\mathrm{bg} = \sqrt{238^2/N_\mathrm{a} + 0.8^2}\,\mathrm{nm}^2$; black circles – random BG points, with a fit (black dotted line) $\hat{\sigma}_\mathrm{bg} = \sqrt{238^2/N_\mathrm{a} + 4^2}\,\mathrm{nm}^2$. For $r_i = 3\lambda/(4\mathrm{NA})$: Open blue triangles – random BG points, with a fit (black dotted line) $\hat{\sigma}_\mathrm{bg} = \sqrt{143^2/N_\mathrm{a} + 1.5^2}\,\mathrm{nm}^2$; filled blue triangles – from out-of-band noise. Deconvolution for $\zeta = 1$: Green diamonds – random BG points, with a fit (green short dashed line) $\hat{\sigma}_\mathrm{bg} = \sqrt{200^2/N_\mathrm{a} + 0.65^2}\,\mathrm{nm}^2$.

We can estimate the RMS shot-noise of the cross-section analyzed with $r_\mathrm{i} = 3\lambda/(2\mathrm{NA})$ to be

$$\hat{\sigma}_\mathrm{n} = \frac{3\lambda d_\mathrm{px}}{2M\mathrm{NA}}\sqrt{\frac{\pi}{N_\mathrm{a}N_\mathrm{fw}}}, \qquad (1)$$

with $d_\mathrm{px} = 6.5\,\mu\mathrm{m}$ the pixel pitch, and $\lambda = 0.55\,\mu\mathrm{m}$, as detailed in the appendix Sec. D. Evaluating Eq.(1), we expect $\hat{\sigma}_\mathrm{n} = 22\,\mathrm{nm}^2$ for $N_\mathrm{a} = 128$, and $\hat{\sigma}_\mathrm{n} = 0.7\,\mathrm{nm}^2$ for $N_\mathrm{a} = 128000$. One way of determining the measurement noise is to measure the extinction in regions with no obvious particles (see appendix Sec. B). The result is shown in Fig. 3b by the open black circles. We see that the expected scaling with $1/\sqrt{N_\mathrm{a}}$ is found, down to a limit of around $4\,\mathrm{nm}^2$ (see black dotted line). We attribute this limit to remaining glass surface roughness,

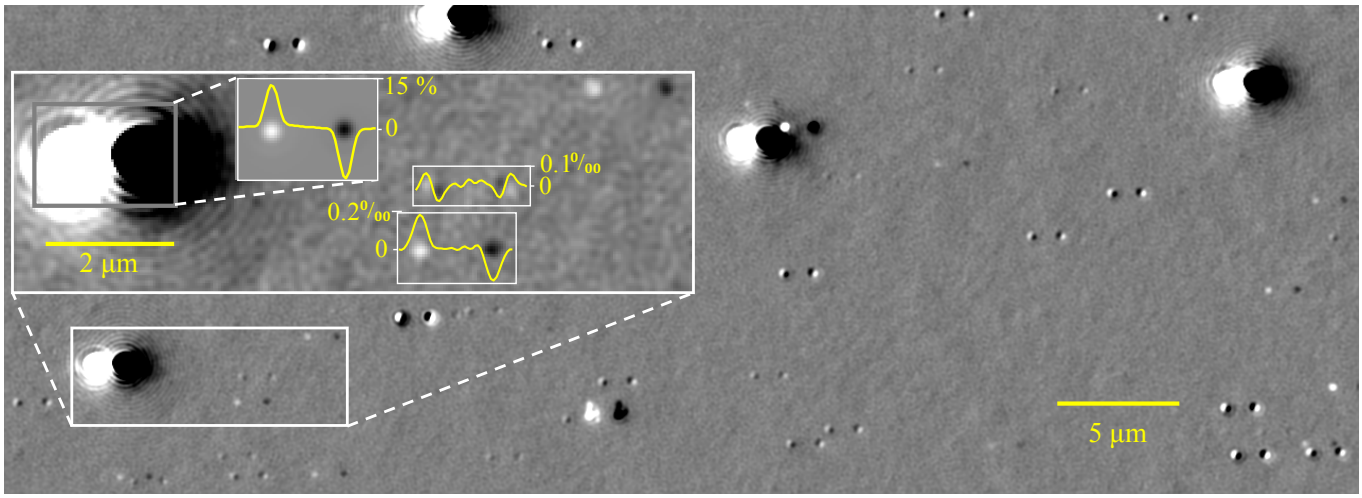

FIG. 4. Full size Δ_1 image (1279 × 460 pixels), showing a sample region of $(55.4 \times 19.9)\,\mu\mathrm{m}^2$. The large inset shows a zoom containing a 60nm GNP, two 5nm GNPs, and a dielectric debris. Line-cuts through the particles are shown as yellow overlays. Grayscale ranges of the images are: main image from -0.3‰ (black) to 0.3‰ (white), large inset from -0.22‰ to 0.21‰, 60nm GNP inset from -0.18 to 0.15.

and effects of the second oil glass interface (see appendix Sec. C), and call it $\hat{\sigma}_{\mathrm{sp}}$, with the measurement noise given by $\hat{\sigma}_{\mathrm{bg}} = \sqrt{\hat{\sigma}_{\mathrm{sp}}^2 + \hat{\sigma}_{\mathrm{n}}^2}$. The corresponding "mottling" is visible in the image and is sample dependent, as can be seen in Fig. 2b,c, where the arrows indicate that the mottling is a differential in the shift-reference direction. To determine the intrinsic measurement noise for a homogeneous sample, we used two alternative methods. Firstly, we used a pair of sequential measurements at a large number of BG positions, and determined $\sqrt{2}\,\hat{\sigma}_{\mathrm{n}}$ from the root mean square difference of the pair of timepoints over all of the BG points. The result is given as red circles in Fig. 3b, along with a fit. We see that there is still some deviation from the $1/\sqrt{N_{\mathrm{a}}}$ scaling as the sensitivity approaches $1\,\mathrm{nm}^2$, and a fit (red dashed line) shows a limit of $0.8\,\mathrm{nm}^2$, which is attributed to remaining drift between the two measurements. An alternative way to measure the shot noise in the images is to use their noise at spatial frequencies out of the transmission band of the imaging system, i.e. at frequencies larger than $2\mathrm{NA}/\lambda$, since these are not affected by the sample structure. This method was also proposed to quantify the photoelectron number in images [11], and is detailed in the appendix Sec. E. The resulting $\hat{\sigma}_{\mathrm{n}}$, shown by the black circles in Fig. 3b, has a shot-noise scaling with no appreciable limit, reaching $0.64\,\mathrm{nm}^2$ at $N_{\mathrm{a}} = 128000$, in good agreement with the value estimated above using Eq.(1).

A. In-band filtering

The known transmission band of the imaging system can also be used to reduce the noise in the Δ images, both for the identification of particles and in the subsequent determination of σ_{ext}. Removing out-of-band components from the measured image data results in the extinction images shown in the right column of Fig. 3a, exhibiting less noise and a finite spatial correlation reflecting the resolution of the imaging system. Note that a high magnification M is advantageous to reduce the noise, see Eq.(1), essentially since a diffraction limited image of the NP covers more pixels, allowing for detection of more photoelectrons at full well capacity within the diffraction limited spot. At the same time, it extends the Nyquist limit of the image well above the spatial frequency transmission band of the imaging system, increasing the out-of-band range. In our case, the detection Nyquist frequency $M/(2d_{\mathrm{px}}) \approx 11.5/\mu\mathrm{m}$, is about twice the imaging bandwidth, $2\mathrm{NA}/\lambda \approx 5.3/\mu\mathrm{m}$. To locate particles in our automated image analysis [8, 10], we identify local maxima above a user-defined threshold, as detailed in the appendix Sec. B. Hence, the noise reduction by the in-band filtering allows for identification of particles with a smaller cross-section. Furthermore, we determine the cross-section using a disk-shaped integration area, A_{i}. This shape contains out-of-band Fourier components, meaning that out-of-band noise affects the resulting σ_{ext}. Indeed, the integration is a convolution of the Δ image with A_{i}, which in Fourier domain corresponds to a multiplication. Out-of-band Fourier components of A_{i} thus mix out-of-band noise into the resulting σ_{ext}. Applying the in-band Fourier filter to the image data first, therefore eliminates these components. The importance of this effect depends on the disk size and the ratio between Nyquist limit and imaging bandwidth, as discussed in detail in the appendix Sec. F. It is typically a small effect, reducing $\hat{\sigma}_{\mathrm{n}}$ in our case by 1.6%.

A full size in-band filtered image of Δ_1 for $N_{\mathrm{a}} = 128000$ is shown in Fig. 4. The 60 nm GNPs are dominating the contrast, with 3000 times larger cross section than the 5 nm GNPs. The technique therefore shows a large dynamic range, covering 4 orders of magnitude, and the PSF is remarkably localized, achieving this dynamic range across a distance of only about $2\,\mu$m, i.e. 10 optical resolutions. The latter is due to the small lateral coherence length of the illumination, provided by the 1.4NA condenser, suppressing the interference between

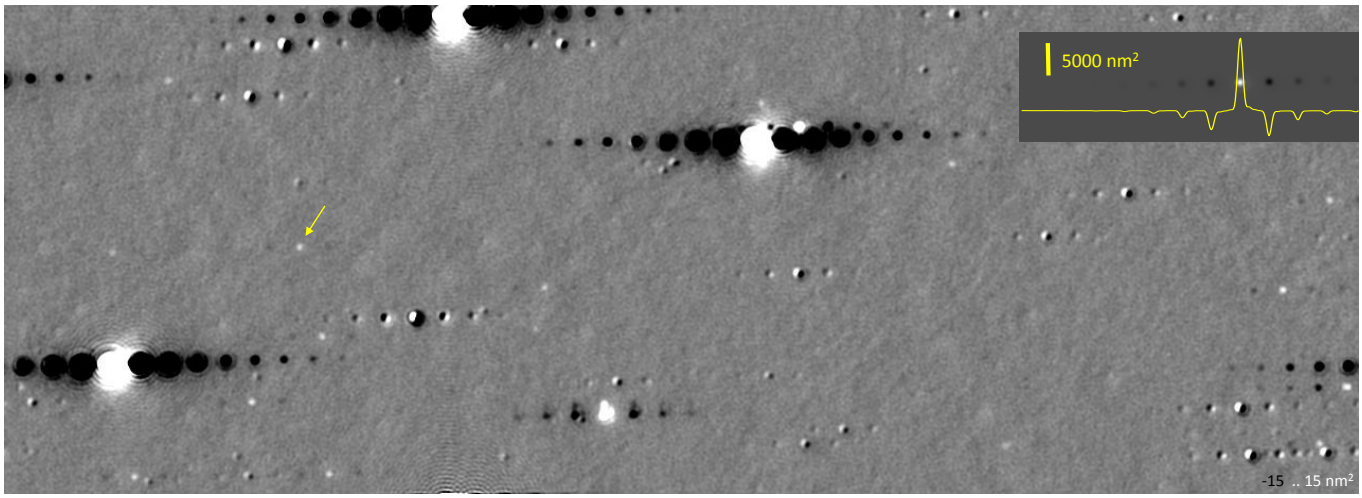

FIG. 5. Extinction cross-section images σ_{ext} of the region shown in Fig. 4, calculated using Wiener deconvolution with $\zeta = 1$. Grey scale from -15 nm^2 (black) to 15 nm^2 (white). A 5 nm GNP is indicated by a yellow arrow. In the top right a region around a 60 nm GNP is shown on a grey scale from -4500 nm^2 to 11020 nm^2 to cover its full response. A horizontal line cut through the GNP is shown as yellow line with a vertical scale as indicated.

the light scattered by the particle and the laterally displaced transmitted light. A zoom region is shown as an inset of Fig. 4, with linecuts across a 60 nm GNP, a 5 nm GNP, and a dielectric debris. The dielectric debris can be identified by its changing sign of contrast across the PSF, resulting in an integrated σ_{ext} close to zero. The specific asymmetric shape, which is conserved between different debris, is attributed to residual optical aberrations in the imaging. We note that this image has an area sufficient to host a few hundred distinguishable NPs, and using the full frame of the camera would increase this number to above a thousand. This allows to extract a detailed NP statistics from a single field of view, acquired within minutes.

With the shot-noise limit in the sub-nm^2 range, the measurement of σ_{ext} on the present sample is limited by the influence of the BG sample inhomogeneity to $\hat{\sigma}_{\text{sp}} = 4\,\text{nm}^2$ for the analysis method used up to now, as shown in Fig. 3b as open black circles. We can reduce the effect of this inhomogeneity on the analyzed σ_{ext} by assuming point-like particles (i.e. particles much smaller than the optical resolution), and refining the analysis procedure as follows. The choice of $r_i = 3\lambda/(2\text{NA})$ in the analysis ensures that the particle extinction cross-section is captured entirely, but its rather large size makes it susceptible to longer range spatial noise, as can be seen in the resulting σ_{ext} image in the appendix Fig. 9. Choosing half of this size, $r_i = 3\lambda/(4\text{NA})$, halves the shot noise, and still captures 83% of the extinction as measured on 60 nm GNPs. Importantly, after correcting for this, $\hat{\sigma}_{\text{sp}}$ is reduced to about 1.5 nm^2, while the shot-noise reaches $\hat{\sigma}_{\text{n}} = 0.38\,\text{nm}^2$, as is shown in Fig. 3b as solid blue triangles. The corresponding image is given in the appendix Fig. 12. This is a significant improvement, showing that the spatial BG can be suppressed by using smaller areas of analysis.

B. Wiener-deconvolution

To reduce the measurement area to the minimum, we developed an analysis method based on Wiener-deconvolution [12], considering the effect of the shifted referencing. The two measured images, I_{S} and I_{R}, are shifted by $\mp\mathbf{d}/2$ in real space, with the shift vector $\mathbf{d}$. Approximating $\Delta_2 = -\Delta_1$, which holds for $\Delta \ll 1$, the Fourier-domain response in Δ_1 is $h(\mathbf{k}) = -2i\sin(\mathbf{kd}/2)$, with the wavevector $\mathbf{k}$. To correct for this response, we perform a Wiener deconvolution in Fourier domain, by multiplying Δ_1 by $g = 1/(h + 1/(\zeta h^*))$, using an estimated signal-to-noise ratio ζ of the data. The resulting deconvolved, in-band filtered images Δ_ζ are given in Fig. 5 for $\zeta = 1$, and for $\zeta = 3$, and 10 in the appendix Fig. 15.

The deconvolution results in a symmetric spatial response with a central peak surrounded by a chain of dips, spaced by the shift distance, as is evident for the 60 nm GNPs, and given by a line-cut in Fig. 5. With increasing ζ, the dip amplitude decreases while the extension of the chain increases, so that the integral of the response function remains zero as determined by the shift method. The resulting extended spatial response requires a somewhat larger distance between particles in the shift direction for quantitative analysis. For the 5 nm GNPs, having a much lower extinction, the dips are close to the noise floor. Furthermore, with increasing ζ, a stripe-like noise pattern along the shift direction is appreciable, a result of the amplification of the noise close to the zeros of the transfer function $h(\mathbf{k}) = -2i\sin(\mathbf{k}\cdot\mathbf{d}/2)$, specifically for $\mathbf{k}\cdot\mathbf{d} \approx 0$.

Using the deconvolved, in-band filtered Δ_ζ, we determine the particle cross-sections simply from the peak values. To calibrate Δ_ζ in terms of σ_{ext}, we use a 60 nm GNP which can be measured reliably with the $r_i = 3\lambda/(2\text{NA})$ method. The resulting $\hat{\sigma}_{\text{bg}}$ for $\zeta = 1$ versus N_{a} is given in Fig. 3b as diamonds, showing a spatial BG of $\hat{\sigma}_{\text{sp}} = 0.65\,\text{nm}^2$, and a shot-noise down to

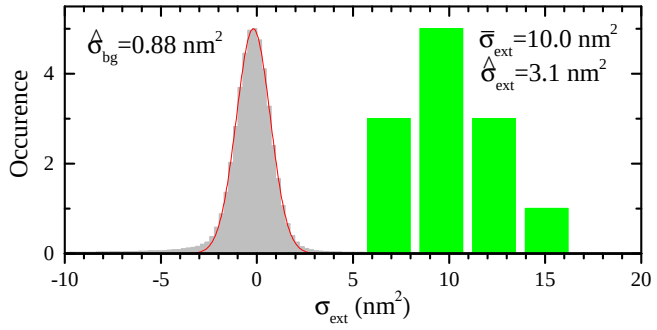

FIG. 6. Histogram of $\sigma_{\rm ext}$ for twelve 5nm GNPs (green bars) seen in the $55\,\mu$m $\times 20\,\mu$m region of the sample shown in Fig. 4, analyzed using deconvolution with $\zeta = 1$. The grey distribution centered at zero is the histogram of the deconvoluted image, and the red line is a Gaussian fit determining the corresponding BG noise $\hat{\sigma}_{\rm bg}$.

$\hat{\sigma}_{\rm n} = 0.56\,{\rm nm}^2$. More details on the calibration and the dependence on the results on ζ are given in the appendix Sec. G.

The deconvolution analysis thus gives the lowest $\hat{\sigma}_{\rm bg}$ and is therefore used to measure the 5 nm GNP (for the corresponding results using the r_i method see appendix Sec. H). The resulting statistical data for the twelve 5 nm GNPs in the image of Fig. 4 are given in Fig. 6. The measured mean cross-section for the GNPs of $\bar{\sigma}_{\rm ext} = 10.0\,{\rm nm}^2$ is consistent with literature [13]. The standard deviation $\hat{\sigma}_{\rm ext} = 3.1\,{\rm nm}^2$ is attributed to the size distribution of the GNPs, as it is significantly above the RMS error $\hat{\sigma}_{\rm bg} = 0.88\,{\rm nm}^2$ of the measured $\sigma_{\rm ext}$ for each individual NP. Using the scaling of $\sigma_{\rm ext}$ with the GNP volume, this corresponds to a relative size distribution of 10%, which is consistent with the manufacturer specification of below 15%.

Apart from the statistical error of the measured $\sigma_{\rm ext}$ given by $\hat{\sigma}_{\rm bg}$, determining its precision, there are also systematic errors, which affect its accuracy. These are relative errors and are relevant for $\sigma_{\rm ext} \gg \hat{\sigma}_{\rm bg}$. They are found to be in the 1–10% range, depending on the analysis method used and the NP measured, as is detailed in appendix Sec. J

V. CONCLUSION

We have shown quantitative extinction measurements of single GNPs with a sub-nm^2 sensitivity in a simple wide-field microscopy modality, using positioning control and an sCMOS camera. As application example, we have determined the size distribution of 5 nm nominal diameter GNPs. The method has thus a sensitivity competitive with more complex laser- and modulation-based techniques, while at the same time enabling rapid acquisition of $\sigma_{\rm ext}$ on many individual particles at once, reducing overall experiment time and enabling a statistically significant characterization of the NPs. This is particularly important, considering that NPs are often fabricated with large size and shape distributions. Notably, the method is applicable to any NP (including dielectric or semi-conducting), and can be easily and cost-effectively implemented on a conventional wide-field microscope. We emphasize that the sensitivity is ultimately limited only by the number of photoelectrons detected, as given in Eq(1). Using a higher magnification, and a camera with higher full well capacity, decreases the number of frames needed, and thus decreases the measurement time required for a given sensitivity. Using for example the parameters of a recently released CMOS camera chip (CMOSIS CSI2100), with 1440×1440 pixels of 2 Me full well capacity and 550 frames per second, a shot noise limit of $0.1\,{\rm nm}^2$ can be obtained within one second, over an area of $100\,\mu{\rm m}^2$, sufficient to detect up to 100 particles. This estimate highlights the potential of reaching single molecule sensitivity with the wide-field approach. The presented wide-field method thus paves the way towards a simple, yet quantitative, highly sensitive, and high-throughput single particle optical characterization.

ACKNOWLEDGMENTS

This work was supported by the UK EPSRC Research Council under grant EP/I005072/1, EP/I016260/1, EP/K503988/1, EP/M028313/1, and the Welsh Government funded project LSBF/R6-005. The authors thank A. Zilli for discussions. The analysis program used is available as ImageJ plug-in at http://langsrv.astro.cf.ac.uk/Crosssection. The data presented in this work are available from the Cardiff University data archive [14].

Appendix A: Full size Δ for different referencing methods

The full size Δ_1 images corresponding to the partial images shown in Fig. 2a,b are given in Fig. 7 and Fig. 8, respectively. In particular, note the long range horizontal banding seen in Fig. 7 which is absent in Fig. 8.

Appendix B: Selecting random background locations

In order to find areas of the image free of particles, we first use the "Find Maxima" function of ImageJ. This function locates peaks in the image, which are above a certain threshold value compared to their surrounding. This value is a parameter chosen by the user, typically a few times larger than the noise level in the image. Once the peaks are found, randomized coordinates are provided to the software, which then checks that none of these are within $2r_{\rm i}$ of any of the peaks found by the ImageJ function. A measurement is then performed, as if there were a particle, at each verified, random BG location.

Appendix C: Statistics of the cross-section analysis

To investigate the origin of the spatial background fluctuations leading to $\hat{\sigma}_{\rm sp}$, we have analyzed the extinction

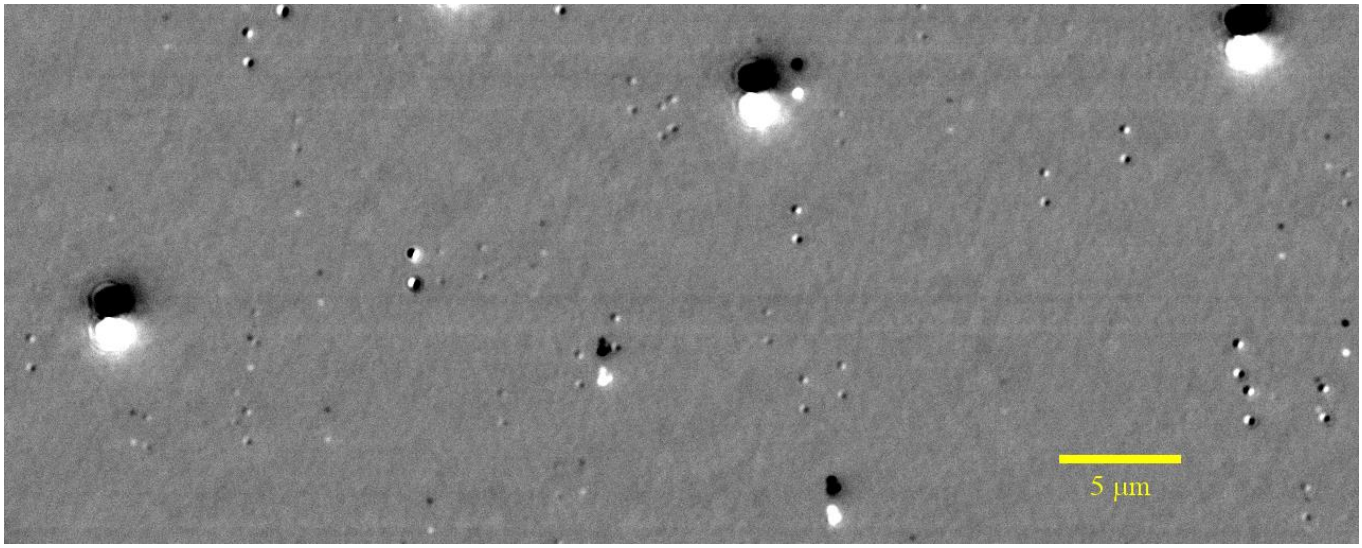

FIG. 7. Δ_1 image for rapid referencing, using $N_\mathrm{d} = 256$, and $N_\mathrm{a} = 128000$. A part of this data is shown in Fig. 2b. Image resolution is 1279×460 pixels, showing an area of approximately $(55.4 \times 19.9)\,\mu\mathrm{m}^2$. A scalebar is given. Grayscale range from -0.3‰(black) to 0.3‰(white).

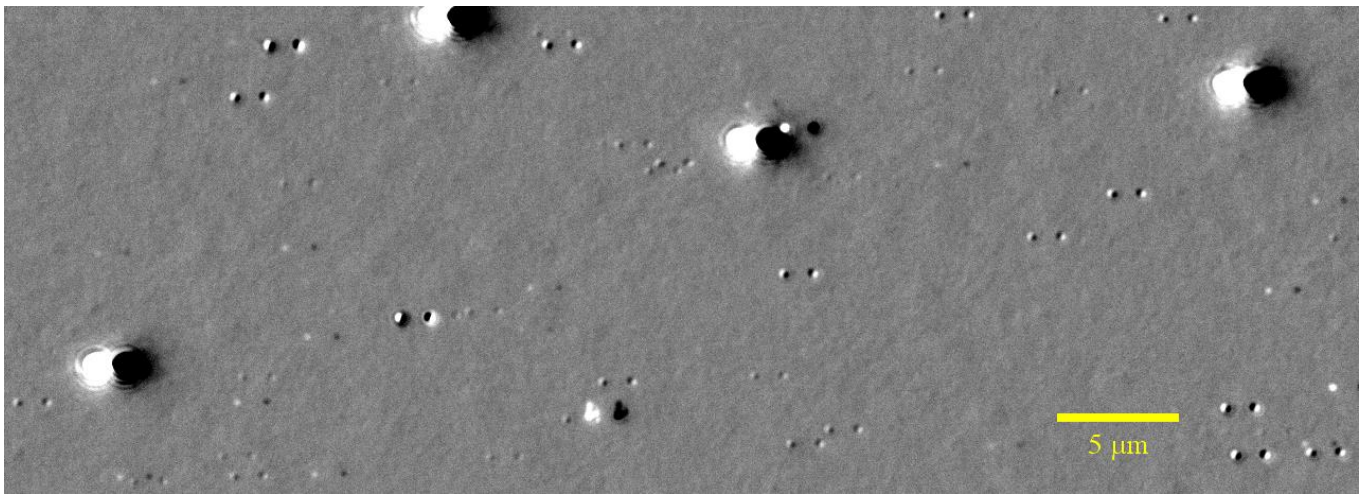

FIG. 8. Δ_1 image for rapid referencing and additional sample motion, using $N_\mathrm{d} = 256$, and $N_\mathrm{a} = 128000$. A part of this data is shown in Fig. 2c. Image resolution is 1279×460 pixels, showing an area of approximately $(55.4 \times 19.9)\,\mu\mathrm{m}^2$. A scalebar is given. Grayscale range from -0.3‰(black) to 0.3‰(white).

using every pixel of the image as center position, by convoluting the in-band filtered Δ with the pair of measurement areas $A_\mathrm{i}(P_{1,2})$, resulting in the image of σ_ext shown in Fig. 9 for $r_i = 3\lambda/(2\mathrm{NA})$ and in Fig. 12 for $r_i = 3\lambda/(4\mathrm{NA})$. The analysis results in a triplet structure for single particles. To evaluate the variation in background regions, we show in Fig. 10 a histogram of σ_ext of this image. The histogram shows a peak around zero, which fitted with a Gaussian, results in a standard deviation $\hat{\sigma}_\mathrm{bg} = 3.82\,\mathrm{nm}^2$ and center $-0.61\,\mathrm{nm}^2$. Deviations from the Gaussian are visible as tails on both sides.

To discuss these tails, we show in Fig. 11 the histogram created by a single 60 nm GNP. The triplet structure results in a peak at positive σ_ext, here at around $11500\,\mathrm{nm}^2$, which represents the actual σ_ext of the GNP. A peak at minus half this value, with twice the occurrences, results from the two side-disks corresponding to the GNP position shifted by $\pm d$, into the reference regions of the analysis. Weakly absorbing background particles thus are expected to result in tails of the histogram in Fig. 10, with the one for positive σ_ext being shallower and more extended than one for negative σ_ext. This is consistent with the observed shape. The image of σ_ext in Fig. 9 shows also regions of wave-like background. This could be due to the influence from out-of-focus particles, which we expect in our sample, from the second glass surface separated by an about $2\,\mu$m layer of oil. Their Fresnel diffraction patterns are able to generate the observed wave-like patterns.

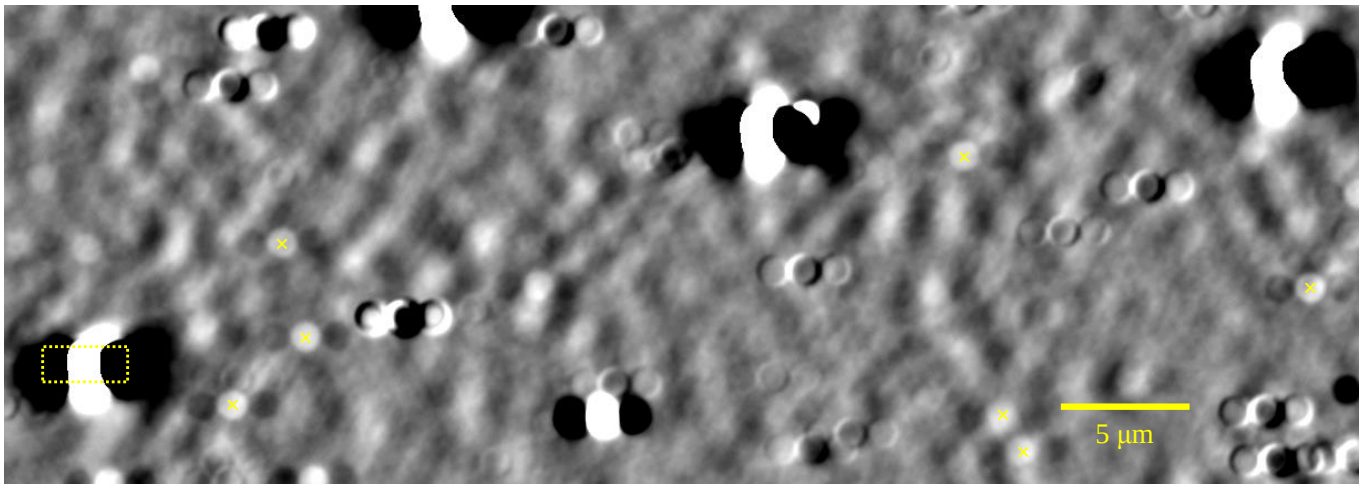

FIG. 9. Extinction cross-section σ_{ext}, evaluated for particles centered at each point of the image, using $r_i = 3\lambda/(2\mathrm{NA})$. Grey scale from -15 nm^2 (black) to 15 nm^2 (white). Scale bar as given. The dashed region is dominated by a 60 nm GNP and its histogram is given in Fig. 11. The characteristic triplet structure of the shifted reference method is visible. The centers of selected 5 nm GNPs are indicated by yellow crosses

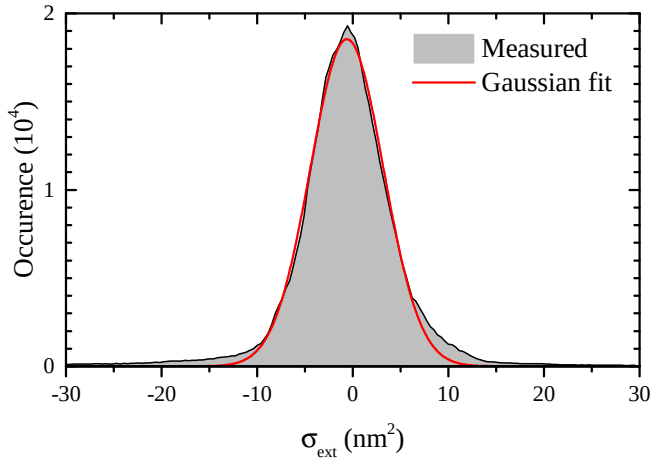

FIG. 10. Histogram of σ_{ext} shown in Fig. 9, in the range close to zero extinction. A Gaussian fit of standard deviation $\hat{\sigma}_{\mathrm{bg}} = 3.82\,\mathrm{nm}^2$ and centre $-0.61\,\mathrm{nm}^2$ is shown by the red line.

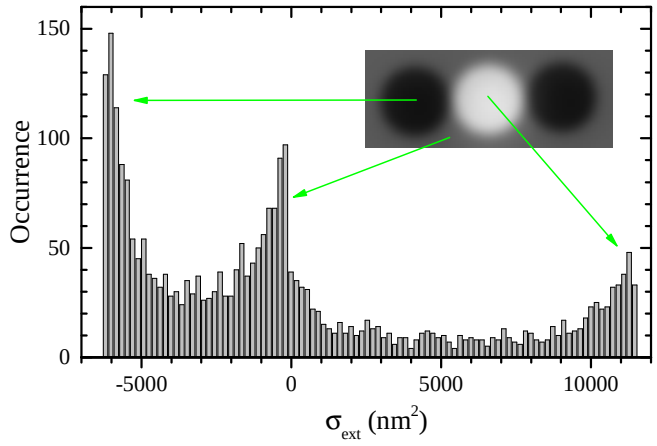

FIG. 11. Histogram of σ_{ext} over the region dominated by a 60 nm GNP as indicated in Fig. 9. The inset shows the shape of the corresponding σ_{ext} image.

Referencing method	Factor
Double ring	$\sqrt{8/3} \approx 1.63$
Shift	1
Shift and double ring	$\sqrt{4/3} \approx 1.15$

TABLE I. Prefactors to equation Eq.(1) for different referencing methods.

Appendix D: Shot-noise limit

We have estimated the RMS shot-noise of the analyzed cross-section in [8] as

$$\hat{\sigma}_{\mathrm{n}} = \frac{3\lambda d_{\mathrm{px}}}{2M\mathrm{NA}}\sqrt{\frac{\pi}{N_{\mathrm{a}}N_{\mathrm{fw}}}}, \tag{D1}$$

with $d_{\mathrm{px}} = 6.5\,\mu$m the pixel pitch, and $\lambda = 0.55\,\mu$m. This estimate is not considering noise due to referencing. Accounting for the noise in the reference image I_{R} adds a factor of $\sqrt{2}$. Using the double ring method with $2r_{\mathrm{i}}$ for the background determination Δ_b adds a factor of $\sqrt{4/3}$. The shifted reference method provides two independent measurements, adding the factor $1/\sqrt{2}$. Depending on the referencing method, we thus pick up additional factors on the order of one, as summarized in Table I. In the shifted reference method the factor is unity, as used in the main manuscript Eq.(1).

Appendix E: Noise estimation using out-of-band signal

To estimate the noise from the out-of-band signal, we Fourier-filter the Δ images, removing components with spatial frequencies lower than $2\mathrm{NA}/\lambda$, which contain additional to the shot noise also image related contrast since they are transmitted by the imaging system. Once filtered, we evaluate the standard deviation, σ, of the pixels. To correct for the missing in-band shot-noise, we cal-

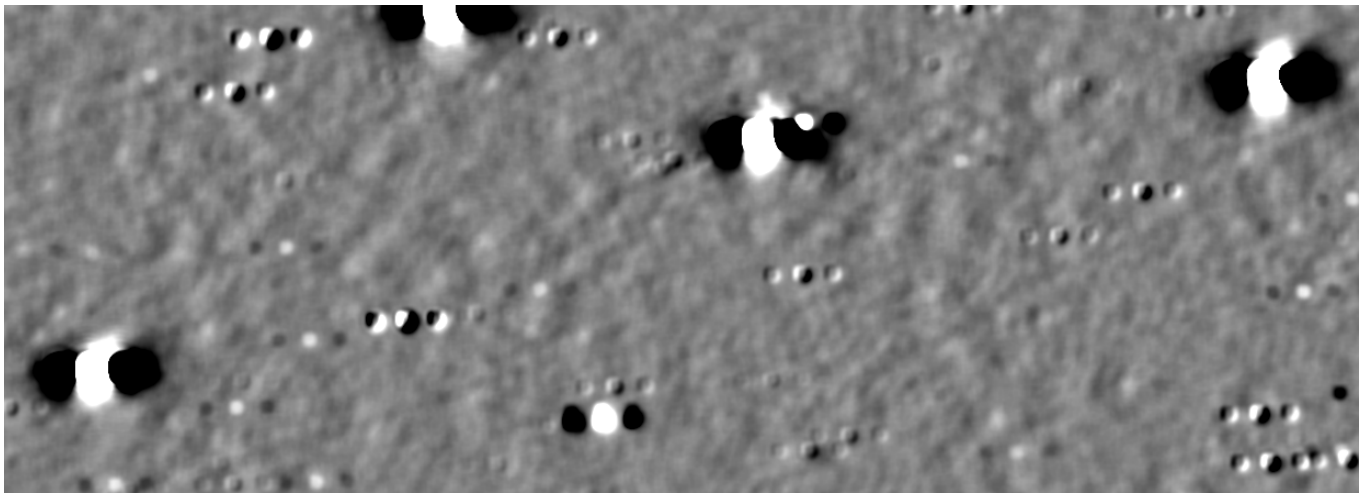

FIG. 12. Extinction cross-section $\sigma_{\rm ext}$, evaluated for particles centered at each point of the image, using $r_i = 3\lambda/(4\mathrm{NA})$. Grey scale from -15 nm^2 (black) to 15 nm^2 (white).

culate the remaining fraction (assuming a Nyquist bandwidth larger than the transmission bandwidth)

$$F = 1 - \frac{4\pi \mathrm{NA}^2 d_{\rm px}^2}{M^2\lambda^2} \tag{E1}$$

of pixels in Fourier domain, allowing us to determine the corrected pixel noise $\sigma' = \sigma/\sqrt{F}$. From this pixel noise of Δ, we find the noise of the resulting extinction by adding the noise from all pixels within A_i, yielding, similar to Eq.(D1),

$$\hat{\sigma}_{\rm n} = \frac{3\lambda d_{\rm px}}{2M\mathrm{NA}}\sqrt{\pi}\sigma' \,. \tag{E2}$$

Appendix F: Extinction noise reduction due to in-band filtering of Δ

We determine the cross-section using a disk-shaped integration area, $A_{\rm i}$. This shape has a sharp edge, and thus contains out-of-band Fourier components. The integration of A_i used to determine $\sigma_{\rm ext}$ is a convolution of the Δ image with $A_{\rm i}$, which at the particle positions provides $\sigma_{\rm ext}$ for the particles. In Fourier domain, the convolution corresponds to a multiplication, so that the out-of-band Fourier components of $A_{\rm i}$ allow the out-of-band noise of Δ to affect the resulting $\sigma_{\rm ext}$. Applying the in-band Fourier filter to the Δ images eliminates these noise components. The amount of noise removed by the in-band filtering depends on the ratio

$$\beta = \frac{r_i 2\mathrm{NA}}{\lambda} \tag{F1}$$

between the radius of A_i and the optical resolution, and on the ratio

$$\gamma = \frac{M\lambda}{\mathrm{NA}d_{\rm px}} \tag{F2}$$

between the imaging band-width and the Nyquist limit. While, in principle, the effect can be expressed analytically to some extent, we chose here numerical simulations to provide the relevant dependencies.

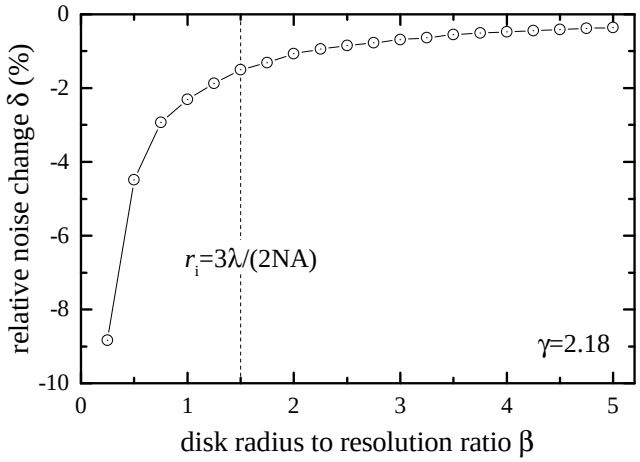

FIG. 13. Relative noise change δ by in-band filtering as function of β, the ratio between the radius of A_i and the optical resolution. $\gamma = 2.18$. The dashed line indicates the radius $r_{\rm i} = 3\lambda/(2\mathrm{NA})$ yielding $\beta = 1.5$ used in the experiments shown in this paper.

The simulations use Δ images given by Gaussian randomly distributed data in the form of a 512×512 pixel image, with zero mean and standard deviation σ. The integration area $A_{\rm i}$ is created as an image, which has the value one for $r < r_i$, and zero otherwise. We convolute Δ with A_i to produce a $\sigma_{\rm ext}$ image, and evaluate its standard deviation $\sigma_{\rm R}$. We repeat the same procedure, but including in-band filtering, yielding $\sigma_{\rm F}$, and define the relative change as $\delta = \sigma_{\rm F}/\sigma_{\rm R} - 1$.

The resulting δ is given in Fig. 13 as a function of β, for $\gamma = 2.18$, corresponding to the experimental data in this manuscript. We find that the noise reduction is largest for small β, as expected due to the increasing fraction of out-of band frequencies for decreasing optical resolution relative to A_i. For $\beta = 1.5$ as used in the analysis in this manuscript, we find $\delta = -1.6\%$, so a rather small change.

The dependence of δ on γ, the ratio between Nyquist bandwidth and imaging bandwidth, is given in Fig. 13 for

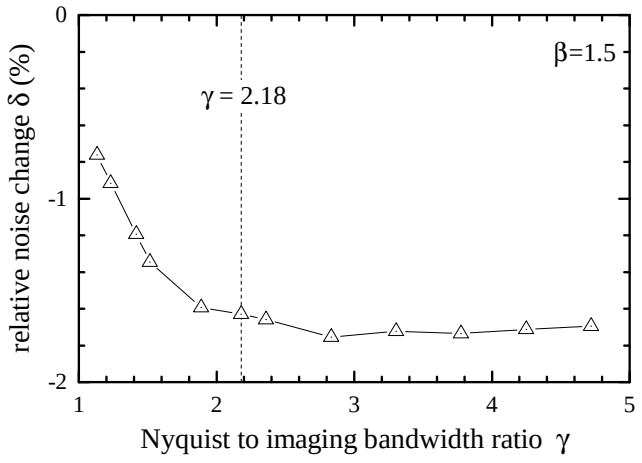

FIG. 14. Relative noise change δ by in-band filtering as function of γ, the ratio between the Nyquist band width and the imaging band width. $\beta = 1.5$. The dashed line indicates the value of γ used in the experiments shown in this paper.

$\beta = 1.5$. We find that the noise reduction is increasing with increasing γ, as expected due to the increasing fraction of out-of band frequencies within the Nyquist band, but is saturating for $\gamma > 2$, at which point most of the out-of band frequencies of A_i are contained within the Nyquist bandwidth.

Appendix G: Wiener deconvolution of Δ

We discuss here the dependence of the results of the Wiener deconvolution on the signal-to-noise parameter ζ. The deconvolved and calibrated images are shown for $\zeta = 1$, 3, and 10 in Fig. 5 and Fig. 15. With increasing ζ the extension of reconstruction artifacts, the chain of dips along the shift-direction, is increasing, but at the same time the depth of the close-lying dips is decreasing. For $\zeta = 1$, two dips are clearly observed around the central peak of the 5 nm GNPs, while they are not visible for $\zeta = 10$. With increasing ζ, a stripe-like noise pattern along the shift direction is appreciable, showing the amplification of the noise close to the zeros of the transfer function $h(\mathbf{k}) = -2i\sin(\mathbf{k}\cdot\mathbf{d}/2)$, specifically for $\mathbf{k}\cdot\mathbf{d} \approx 0$.

The calibration of the cross-section images from the Δ_ζ images was performed using a 60 nm GNP, which has a peak height $\Delta_{\rm pk}$ in the deconvolved Δ_ζ, which is increasing with ζ as shown in Fig. 16. This peak height was scaled to provide the cross-section of the 60 nm GNP determined using the $r_{\rm i} = 3\lambda/(2{\rm NA})$ method. To take into account the rather large contrast of the 60 nm GNP in Δ_1 (see Fig. 4), we used the same approximation as in the deconvolution in this method, i.e. we used $\Delta_2 = -\Delta_1$, which results in a 5% calibration correction compared to using Δ_2 separately calculated, which would yield $\Delta_2 = 1 - 1/(1 - \Delta_1)$.

The resulting statistical properties of the 5 nm GNP ensemble, already shown in Fig. 6 for $\zeta = 1$, are shown in Fig. 16 as a function of ζ. One can see that both $\bar{\sigma}_{\rm ext}$ (green triangles) and $\hat{\sigma}_{\rm ext}$ (error bars) are not significantly varying with ζ. The background noise $\hat{\sigma}_{\rm bg}$ is slowly increasing with ζ, from 0.88 nm^2 for $\zeta = 1$ to 1.14 nm^2 for $\zeta = 10$.

Appendix H: Extinction cross-sections of 5nm GNP and dielectric debris

Here we report the analysis of the 5 nm GNP ensemble shown in Fig. 6, and 16 dielectric particles in the image of Fig. 4, using the $r_{\rm i} = 3\lambda/(2{\rm NA})$ method. The results are given in Fig. 17. With this method, the shot-noise limit $\hat{\sigma}_{\rm n} = 0.65\,{\rm nm}^2$ (dark grey area) is much smaller than the measured noise $\hat{\sigma}_{\rm bg} = 3.3\,{\rm nm}^2$ (light gray area), which is dominated by the background spatial fluctuations $\hat{\sigma}_{\rm sp}$. The measured mean cross-section for the GNPs of $\bar{\sigma}_{\rm ext} = 10.4\,{\rm nm}^2$ and its standard deviation $\hat{\sigma}_{\rm ext} = 2.9\,{\rm nm}^2$ are similar to the values found with the deconvolution method in Fig. 6, despite the much larger $\hat{\sigma}_{\rm bg}$. This is evidence for some anticorrelation between the background and the particle exctinction in the finite ensemble, which is generally not expected. The dielectric particles show an extinction cross-section around zero, as expected, even so their contrast in Δ (see Fig. 4) is exceeding the one of 5 nm GNPs.

Appendix I: Comparison of scanning and widefield extinction methods

Sensitive transmission imaging has been shown using sample scanning in Ref. 6 and 7, while wide-field imaging is shown in the present work. The ultimate limit in transmission imaging is given by the shot-noise of the detected light. Beyond this, there are other limitations affecting scanning and widefield approaches differently.

1. Scan speed

Sample scanning was implemented in Ref. 6 with a closed-loop piezoelectric stage. The dwell time used per 20(40) nm pixel was 1(2) ms in Ref. 6 (Ref. 7), respectively, and 80(10) averages were taken for the images shown, giving total dwell times per pixel of 80(20) ms. Typical piezoelectric scan stages such as the one we use in the present work have step response times on the order of 10 ms. This limits the pixel time to about 0.1 to 1 ms, for a small area, as shown in these works, due to the limitations of the stage dynamics.

The wide-field data shown in Fig. 4 have 588340 pixels. For $N_{\rm a}$=128000, the acquisition takes 1.1 ms per pixel, more than one order of magnitude faster than Ref. 6 and 7. For $N_{\rm a} = 10000$, this reduces to 84 μs per pixel, at a shot noise of 1.5 nm^2, and for $N_{\rm a} = 1000$, to as little as 8.4 μs per pixel (which is not feasible with available piezo-stages, as discussed above) at a shot noise of 4 nm^2, and a total acquisition duration of 5 s. One can estimate that, using a camera, such as the CMOSIS CSI200, with 1440 x 1440 pixels of 2 Me full well capacity, and acquiring at 550 frames per second, a shot noise of 0.03 nm^2 can be obtained within 10 seconds over an area of 100 μm^2. This shot noise value is suitable for single molecule detection

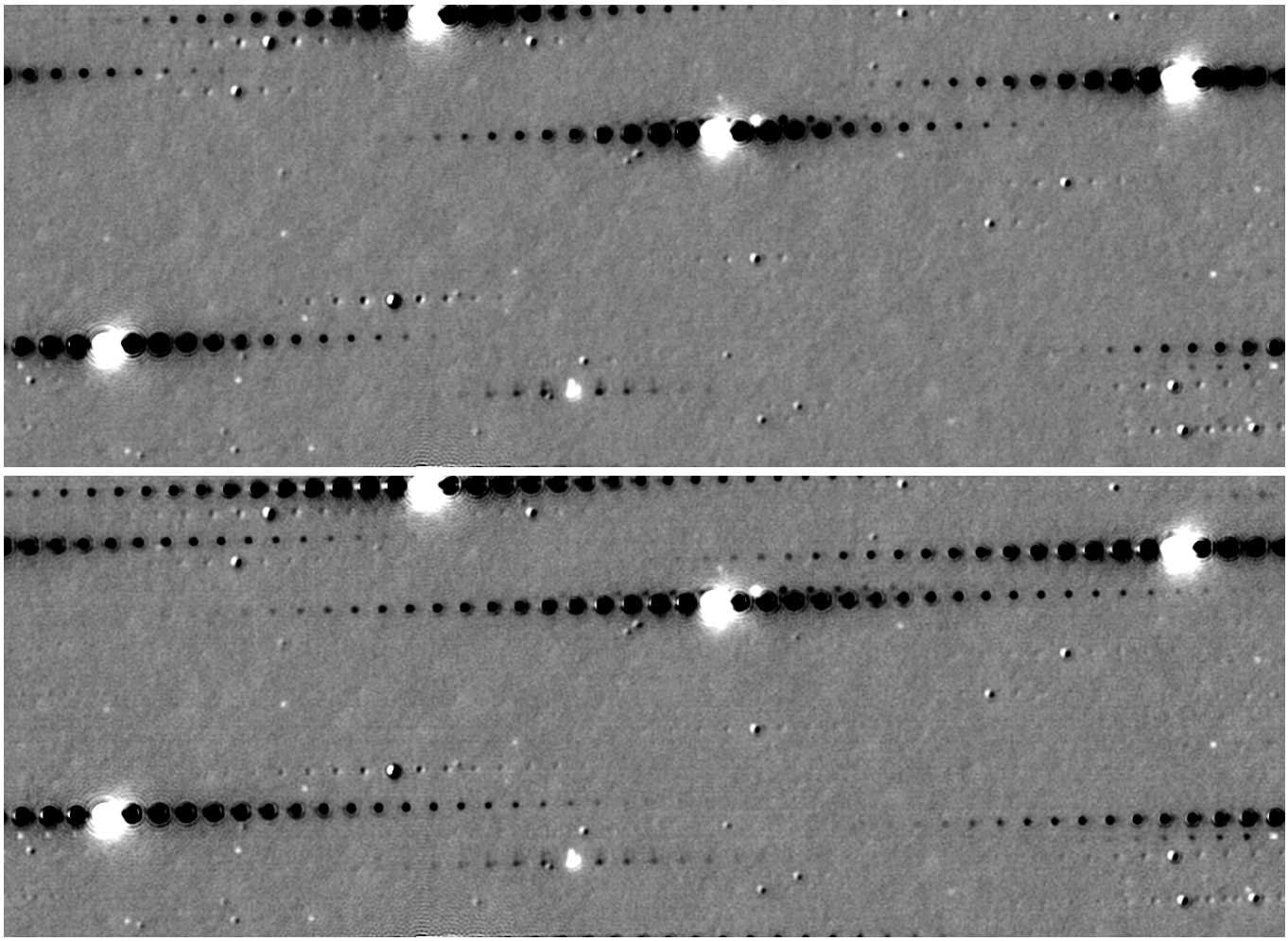

FIG. 15. As Fig. 5, for $\zeta = 3$ (top) and $\zeta = 10$ (bottom).

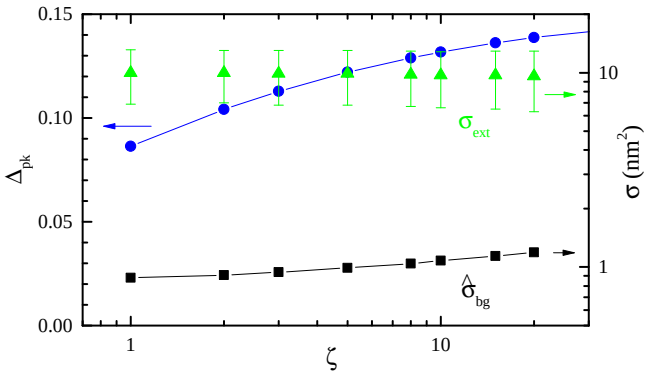

FIG. 16. Results of the deconvolution analysis as function of the employed signal-to-noise ratio ζ. Peak amplitude $\Delta_{\rm pk}$ of a 60 nm GNP (blue disks). Background spatial noise $\hat{\sigma}_{\rm bg}$ (black squares), and extinction statistics of the 5 nm GNP ensemble given by $\bar{\sigma}_{\rm ext}$ (green triangles) with error bars $\pm\hat{\sigma}_{\rm ext}$.

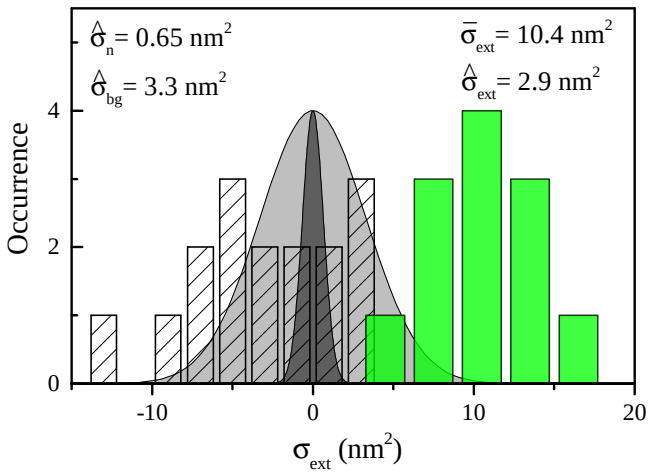

FIG. 17. Histograms of twelve 5nm GNPs, and 16 dielectric particles (debris) seen in the 55 μm $\times$ 20 μm region of the sample shown in Fig. 4. Green bars represent GNPs, and black hatched bars represent dielectric debris. The narrow, dark grey distribution centered at zero represents the shot noise and is characterised by $\hat{\sigma}_{\rm n}$. The wider, light grey distribution shows $\hat{\sigma}_{\rm bg}$.

and is similar to that shown in Ref. 6 and 7, while being about 2 orders of magnitude faster, requiring 0.16 ms per 40 nm pixel.

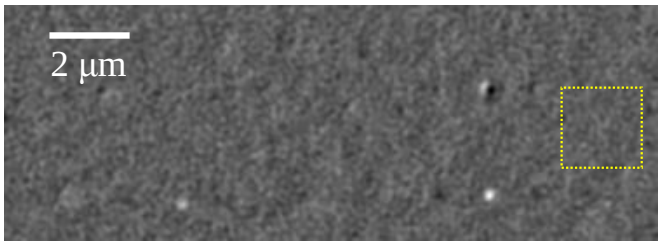

FIG. 18. Selected region of Fig. 5 containing two 5 nm GNP, after applying a high-pass filter removing components with spatial frequencies below $0.5/\mu$m. The yellow dashed square indicates a selected $(2 \times 2)\mu\text{m}^2$ region of low noise.

2. Low-frequency noise

Any experiment shows low frequency noise, also called $1/f$ noise, describing slow drifts, e.g. of thermal nature. These drifts are of different significance in a scanning versus a wide-field approach. In the former, data from different positions are acquired sequentially, so that data are taken temporally separated by up to the total acquisition time. As a result, low frequency fluctuations are important, leading to a characteristic stripe pattern, as typically seen in scanning probe images. In Ref. 6 and 7, multiple frames were averaged, instead of increasing the pixel dwell time, reducing the effect of the $1/f$ noise by the number of averages. Furthermore, a "low-order polynomial baseline subtracted on a line-by-line basis to account for low-frequency fluctuations (10 Hz)" was used.

In the wide-field approach, $1/f$ intensity noise is not relevant if it is homogeneous across the field of view, since all pixels are observed over the same time interval. Only spatially inhomogeneous drift is affecting the result. In our work we have countered the remaining slow drifts by using the shifted referencing method, with a switching frequency of 0.8 Hz, and a registration of the images.

To investigate the effect of a background subtraction over small areas, used in Ref. 6 and 7, we show in Fig. 18 a high-pass filtered region of Fig. 5, where the extinction calibration has been adjusted for the filtering. The high-pass used removed spatial frequencies below $0.5/\mu$m, which have a period larger than $2\,\mu$m, consistent with the image sizes shown in Ref. 7. Choosing a low noise region of $2\,\mu$m size, as indicated, we find a noise of $\hat{\sigma}_{\text{bg}} = 0.69\,\text{nm}^2$. The shot noise in this image was determined from the N_{a} dependence to be $\hat{\sigma}_{\text{n}} = 0.57\,\text{nm}^2$, so that the effect of the residual structure can be estimated to be $\hat{\sigma}_{\text{sp}} = 0.39\,\text{nm}^2$, below the shot noise and about half the value of $\hat{\sigma}_{\text{sp}} = 0.65\,\text{nm}^2$ found for the full image as given in Fig. 3b.

3. Shot-noise limited detection for low power

In the scanning method [6, 7], a diode detector was used. The noise equivalent power (NEP) of this detector is limited by the amplifier noise, which is given by the thermal noise of the feedback resistor and the equivalent input noise of the operational amplifier used. The detector (New Focus Nirvana) has a NEP of $3\,\text{pW}/\sqrt{\text{Hz}}$, according to manufacturer specifications, which is equal to the shot noise of $28\,\mu$W detected optical power, at a wavelength of 633 nm. In [7], a beam of $200\,\mu$W at the sample was used, which, considering the losses of the optics to the detector, is estimated to be about $150\,\mu$W at the detector. At this power, the detector noise is a small contribution, and a noise 2% above the shot noise limit is expected. For the balanced detection used, the shot noise of the reference beam is also measured, resulting in $\sqrt{2}$ times the single beam shot noise limit, assuming balanced powers in signal and reference beam. Using a photon detection efficiency of 50% from sample to detector, the noise in the transmission is estimated as 0.56 ppm for 20 ms integration time. The noise in two subtracted images is reported in [7] to be 0.7 ppm, consistent with the estimated value of $\sqrt{2} \times 0.56\,\text{ppm} \approx 0.8\,\text{ppm}$. For a power of $100\,\mu$W, used in Ref. 6, we estimate a noise of two subtracted images of $\sqrt{2} \times 0.43\,\text{ppm} \approx 0.61\,\text{ppm}$ for 80 ms integration time, again similar to the reported value of 0.53 ppm. At lower powers, however, the detector noise dominates. For example, for $10\,\mu$W at the sample, the noise in the transmission for 80 ms integration time is estimated to be 2.5 ppm, and for $1\,\mu$W we find 22 ppm. To maintain the noise at 0.43 ppm, integration times of 2.7 s, and 209 s, respectively, would be required.

In the wide-field technique reported here, we use a sCMOS camera as detector, which has a read noise of only 2 electrons, enabled by the small capacitance of the on-chip pixel amplifiers. The read noise is thus negligible close to the full-well capacity, and shot noise limited detection is possible also for low power.

4. Power density

In the scanning method, one diffraction limited region is excited at any given time, so that the power density compared to the wide-field technique is increased by the number of resolved regions in the image, about 10^5 for the images we show. High local power density can lead to heating, which is actually the contrast mechanism in photothermal imaging, and can also saturate the absorption of single quantum emitters. A power of $200\,\mu$W as used in Ref. 7, corresponds to a power density of $0.5\,\text{MW}/\text{cm}^2$ for $(0.2\,\mu\text{m})^2$ focus area. Using the reported absorption cross section of the fluorophore TDI of $0.1\,\text{nm}^2$, an excitation rate of 1.6 GHz is calculated, which is five times the radiative rate of 0.3 GHz of TDI. One should therefore expect that the absorption is reduced by a factor of five, and is power-dependent. Since no significant saturation of absorption compared to expectations was observed in Ref. 7, we can conclude that the measured TDI molecules exhibited significant non-radiative recombination, suppressing the absorption saturation. In Ref. 6 Fig. 4, the incident power was $10\,\mu$W, and the detected fluorescence had a rate of about 3 kHz, while the excitation rate is estimated to be 80 MHz. The ratio between detection and excitation rate of 40 ppm is given by the product of emission quantum efficiency, collection efficiency, and detection efficiency. Using a detection efficiency of 20%, and a collection efficiency of 30% for the 1.4NA objective, results in an estimated emission quantum efficiency

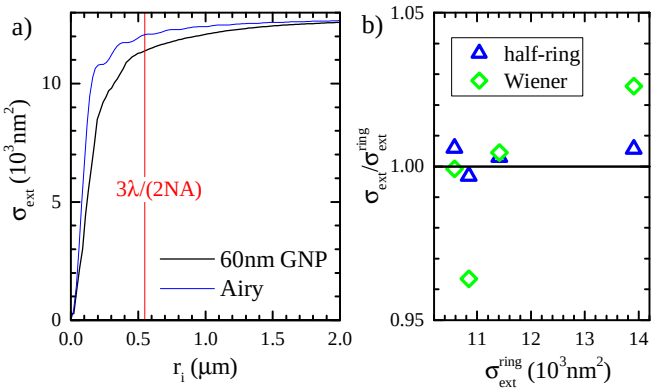

FIG. 19. a) Measured $\sigma_{\rm ext}$ as function of the ring radius r_i for a 60 nm GNP. The integral of an Airy function is given as blue line (see text). b) Variation of the determined $\sigma_{\rm ext}$ using the half-ring and Wiener methods relative to the ring method over the four 60 nm GNPs in Fig. 4.

of 0.06%. This shows that the fluorophore was already bleached in emission. In Ref. 6 Fig. 2, a photon rate of 1 MHz is found for TDI at 100 μW power, yielding an emission quantum efficiency of 2%. This is still much lower than the close-to-unity quantum efficiency of non-bleached TDI. In essence, we find that the scanning techniques of Ref. 6 and 7 use powers in the saturation regime of intact fluorophores, which can lead to systematic errors of the deduced absorption cross-section.

In the wide-field technique, all spatial points are measured at the same time. The required power density is thus much lower. The pixel saturation at full well capacity provides an upper limit of the power used. For the reported setup, pixel readout rates are about 300 MHz at 30 ke per pixel, resulting, for 50% detection efficiency, in about 10 μW at the sample over the observed field of view of 1279 × 460 pixels. At the resulting power density of 1 W/cm^2, photothermal effects or saturation are irrelevant. Even for the high full well capacity camera parameters mentioned above, for which the required power density is about two orders of magnitude larger, the resulting power density is about three orders of magnitude lower than in the scanning methods.

Appendix J: Accuracy and systematic errors

We have presented three different analysis methods to retrieve $\sigma_{\rm ext}$, called ring, half-ring, and Wiener, and their statistical errors due to shot noise and background roughness have been discussed in detail. These errors define the precision of the method. The systematic errors are determining, on top of the precision, the accuracy. They are relative errors, and therefore relevant only for $\sigma_{\rm ext} \gg \hat{\sigma}_{\rm bg}$. Since the present work explores the sensitivity limit, we will give here only a short discussion, while reserving a detailed characterization as a function of particle shape, size, etc. for a forthcoming work.

An obvious systematic error is due to the collection of a part of the scattered light, in difference to the definition of the extinction cross-section. The objective we used collects about 36% of the solid angle range, so assuming isotropic scattering, the scattering contribution to the measured extinction cross-section is reduced by 36%. This can be corrected if the scattering pattern of the particle is known. For the 5 nm GNPs investigated in the present paper, scattering is negligible, making this error insignificant. For the 60 nm GNPs, scattering is expected to be about 20% of the extinction cross-section, so that the measured extinction is about 93% of the correct value.

The analysis method itself also leads to systematic errors. The ring method integrates up to a given radius. Hence, for a larger radius, we expect a smaller systematic error, but a larger statistical error. In [8] Fig.1b we found that at $r_i = 3\lambda/(2{\rm NA})$ for an 0.95NA objective, $\sigma_{\rm ext}$ was saturated. The observed behaviour will depend somewhat on the objective and NA used, due to the influence of optical errors of the objective, the change of the PSF from a paraxial one to a fully vectorial one for large NA, and the influence of the coherence length of the illumination (in the present data the illumination NA was 1.34, somewhat below the objective NA of 1.45).

To investigate this in the present data, we repeated the analysis for the ring method used here. The result is given in Fig. 19a, showing the dependence of the measured $\sigma_{\rm ext}$ on $r_{\rm i}$ on the 60 nm GNP zoomed in Fig. 4. To enable the evaluation of larger $r_{\rm i}$ in the shifted referencing used, we analyzed the integrals over half-moon disks pointing away from the respective shifted image. We find that for $r_i = 3\lambda/(2{\rm NA}) \approx 548$ nm, we capture about 90% of the value measured for $r_i = 2\,\mu$m. For comparison, we show the integral of an intensity Airy-function $|J_1(x)/x|^2$, with $x = 2\pi r{\rm NA}/\lambda$, normalized to the value at $r = 2\mu$m. We see that the measured data is wider, as expected due to the effects of high NA and partially coherent imaging in transmission.

The half-ring and Wiener methods have been calibrated using the ring method on the 60 nm GNPs. These methods are more reliant on the detailed shape of the PSF. Hence, differences in the PSF for particles are expected to lead to systematic errors. For a small particle in the dipole limit, the PSF shape variations are determined by the anisotropy of the polarizability tensor, which reflects the particle asymmetry. To evaluate the remaining systematic errors of half-ring and Wiener methods in our measurements, we show in Fig. 19b their measured relative error with respect to the ring method for 60 nm GNPs. We find that the deviations are in the 0.5% range for the half-ring method, and in the few % range for the Wiener method.

[1] Dmitri V. Talapin, Jong-Soo Lee, Maksym V. Kovalenko, and Elena V. Shevchenko, "Prospects of colloidal nanocrystals for electronic and optoelectronic applications," Chem. Rev. **110**, 389–458 (2010).

[2] Tianmeng Sun, Yu Shrike Zhang, Bo Pang, Dong Choon Hyun, Miaoxin Yang, and Younan Xia, "Engineered nanoparticles for drug delivery in cancer therapy," Angew. Chem. Int. Ed. **53**, 12320–12364 (2014).

[3] Aurélien Crut, Paolo Maioli, Natalia Del Fatti, and Fabrice Vallée, "Optical absorption and scattering spectroscopies of single nano-objects," Chem. Soc. Rev. **43**, 3921–3956 (2014).

[4] Stéphane Berciaud, Laurent Cognet, Gerhard A. Blab, and Brahim Lounis, "Photothermal heterodyne imaging of individual nonfluorescent nanoclusters and nanocrystals," Phys. Rev. Lett. **93**, 257402–257405 (2004).

[5] A. Arbouet, D. Christofilos, N. Del Fatti, F. Vallée, J.R. Huntzinger, L. Arnaud, P. Billaud, and M. Broyer, "Direct measurement of the single-metal-cluster optical absorption," Phys. Rev. Lett. **93** (2004).

[6] P. Kukura, M. Celebrano, A. Renn, and V. Sandoghdar, "Single-molecule sensitivity in optical absorption at room temperature," J. Phys. Chem. Lett. **1**, 3323–3327 (2010).

[7] M. Celebrano, P. Kukura, A. Renn, and V. Sandoghdar, "Single-molecule imaging by optical absorption," Nat. Phot. **5**, 95–98 (2011).

[8] Lukas M Payne, Wolfgang Langbein, and Paola Borri, "Polarization-resolved extinction and scattering cross-section of individual gold nanoparticles measured by wide-field microscopy on a large ensemble," Appl. Phys. Lett. **102**, 131107–1 (2013).

[9] L.M. Payne, G. Zoriniants, F. Masia, K.P. Arkill, P. Verkade, D. Rowles, W.W. Langbein, and P. Borri, "Optical micro-spectroscopy of single metallic nanoparticles: quantitative extinction and transient resonant four-wave mixing," Faraday Discuss. **184**, 305–320 (2015).

[10] L.M. Payne, *Optical extinction and coherent multiphoton micro-spectroscopy of single nanoparticles*, Ph.D. thesis, Cardiff University (2016).

[11] Rainer Heintzmann, Peter K. Relich, Robert P.J. Nieuwenhuizen, Keith A. Lidke, and Bernd Rieger, "Calibrating photon counts from a single image," arXiv:1611.05654 (2016).

[12] M. Bath, *Spectral Analysis in Geophysics* (Elsevier, Amsterdam, 1974).

[13] M. van Dijk, *Nonlinear-optical studies of single gold nanoparticles*, Ph.D. thesis, Universiteit Leiden (2007).

[14] Cardiff University data archive: http://dx.doi.org/10.17035/d.2017.xxx.